WILEY-VCH

Anti-Fatigue Hydrogel Electrolyte for All-Flexible Zn-Ion Batteries

*Qun Liu, Zhenlu Yu, Qiuna Zhuang, Jang-Kyo Kim, Feiyu Kang, Biao Zhang**

Q. Liu, Z. Yu, Prof. B. Zhang
Department of Applied Physics and Research Institute for Smart Energy
The Hong Kong Polytechnic University, Hung Hom, Hong Kong 999077, China
E-mail: biao.ap.zhang@polyu.edu.hk
Q. Zhuang
Laboratory for Advanced Interfacial Materials and Devices Institute of Textiles and Clothing,
The Hong Kong Polytechnic University, Hung Hom, Hong Kong 999077, China
Prof. J.-K. Kim
School of Mechanical and Manufacturing Engineering, University of New South Wales,
Sydney 2052, NSW, Australia
Prof. F. Kang
Shenzhen Geim Graphene Center, Institute of Materials Research, Tsinghua Shenzhen
International Graduate School, Tsinghua University, Shenzhen 518055, China

Abstract

Hydrogel electrolytes have been widely explored in Zn metal batteries for application in wearable electronics. While extensive studies have been conducted in optimizing the chemical structure and boosting the tensile elasticity, the mechanical stability of the hydrogel under repeated deformation is largely overlooked, leading to unsatisfactory performance at large cycling capacity. We systematically analyze the compressive fatigue-resistance properties of the hydrogel electrolyte, revealing the critical roles of the salts and copolymer matrix on crack initiation and propagation. We show that, on the premise of homogeneous Zn deposition, an improved anti-fatigue property is essential to achieve high-capacity Zn metal anodes. The optimal $Zn(ClO_4)_2$-polyacrylamide/chitosan hydrogel electrolyte (C-PAMCS) exhibits an unprecedented lifespan of 1500 h for Zn//Zn cells at a current density of 10 mA cm^{-2} and a high areal capacity of 10 mAh cm^{-2}. We exemplify the potential application of C-PAMCS in all-flexible Zn-ion batteries enabled by a flexible current collector based on Ag nanowires embedded elastomer.

Keywords: hydrogel, compression, fatigue, flexible, Zn-ion batteries

1. Introduction

The advancement of wearable technologies stimulates the prosperous development of flexible power suppliers.[1] Since good compatibility between the human body and devices is required, toxic organic battery systems are not favorable.[2] Rechargeable aqueous Zn metal batteries have been intensively investigated as promising candidates for the next generation battery systems attributed to their low cost and intrinsic safety.[3] Nevertheless, the parasitic reactions and flagrant dendrite evolution hinder the practical implementation of Zn metal anodes.[4] Rational design of electrolyte composition and structure is one of the promising strategies to realize long-lifespan and highly reversible Zn anodes.[5] Compared to conventional aqueous electrolytes containing irregular ion migration pathways and highly active free water, hydrogel electrolytes with polymeric matrices including sodium alginate (SA),[6] carboxymethyl cellulose (CMC),[7] polyacrylamide (PAM)[8] and gelatin[9] have been verified to be more effective to tackle the Zn metal anode challenges. Specifically, self-corrosion of the Zn anode can be inhibited by reducing free water molecules, while frantic dendrite growth is expected to be suppressed ascribed to interactions between Zn^{2+} and the beneficial functional groups in polymer chains.[10]

The hydrogel electrolyte must possess sufficient mechanical stability for utilization in wearable electronics. Tremendous works have been devoted to boosting the elasticity, particularly at the pristine stage under the tensile test. Considering the long service life of the battery, the anti-fatigue performance should also be taken into account but has been largely overlooked. The repeated charge/discharge of the battery would pose a cyclic loading to the hydrogel electrolyte, potentially promoting the crack initiation and propagation that ultimately leads to the failure of the hydrogel and the cell. We briefly analyze the stress conditions in the coin cell and pouch cell configurations (**Figure 1a**). Generally, to achieve high volumetric energy density, the thickness of the separator is desired to be as thin as possible (usually 20-

1000 μm),[11] on the premise of good mechanical properties. At such a microscopic thickness, the volume change of the battery will produce notable degrees of compression strain to hydrogel electrolytes, which also serve as the separator between the anode and cathode.

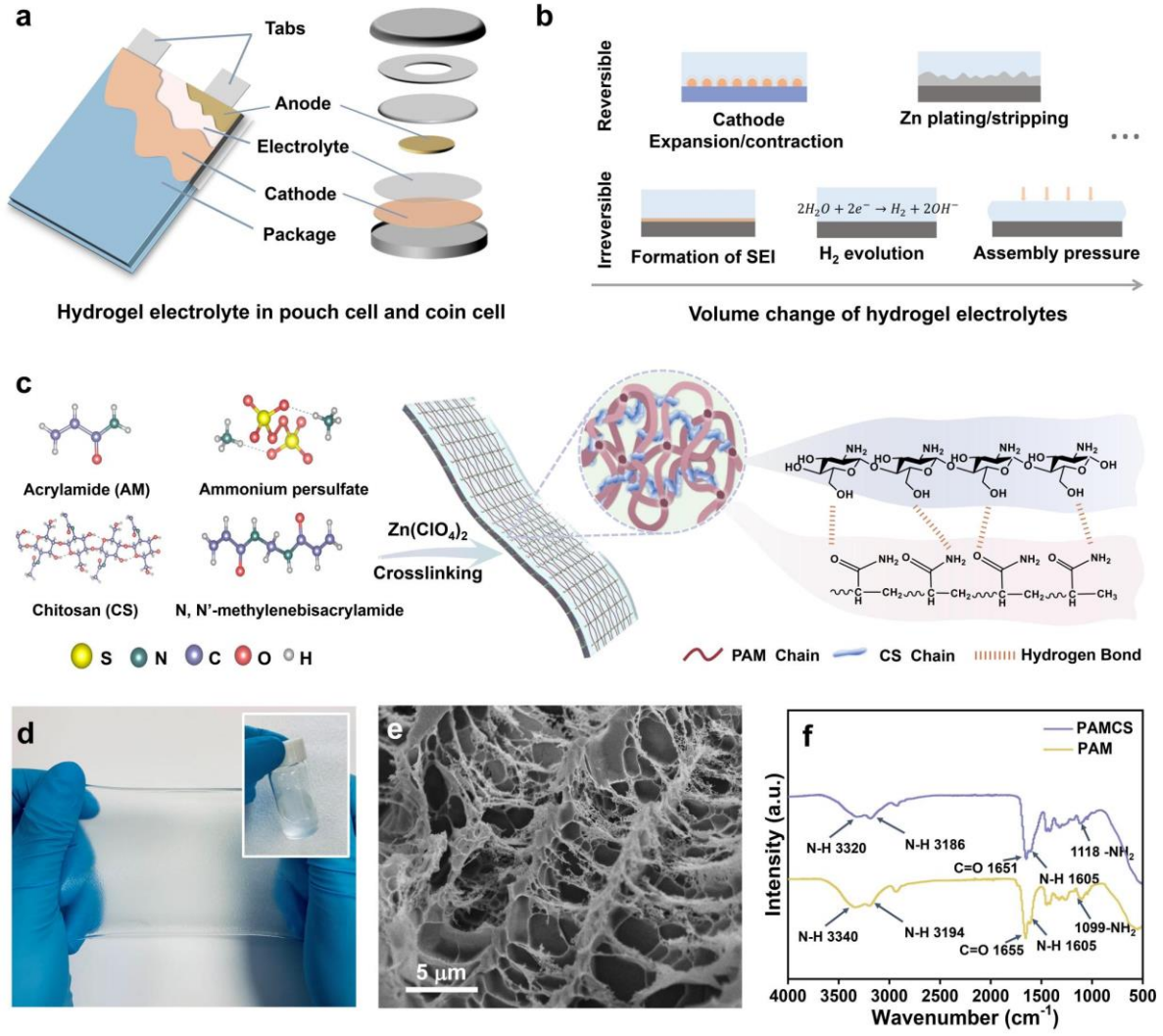

Figure 1. Material synthesis and characterization. (a) Structures of conventional Zn coin cell and pouch cell; (b) The demonstration of volume change of hydrogel electrolyte affected by essential factors; (c) Schematic illustration of preparation process of C-PAMCS; (d) Digital images of precursor and as-prepared C-PAMCS; (e) Cross-sectional SEM images of freeze-dried C-PAMCS and (f) FT-IR spectrum of C-PAM and C-PAMCS matrix.

As illustrated in **Figure 1b**, two types of deformation will be induced to the hydrogel electrolyte during the assembly and operation of the cells, including i) irreversible deformation

occurs under abusive conditions, such as deformation during cell assembly to ensure the close interfacial contact with Zn anode, H_2 evolution reactions and solid electrolyte interphase (SEI) formation during the initial cycle. As a reference, the glass-fiber separator (GF/D, Whatman) of 1 mm will be compressed to nearly 200 μm when the coin cell is assembled under a pressure of 50 kg cm^{-2} (**Figure S1**); ii) reversible deformation accompanied by the volume changes of cathode and anode in the cyclic charging and discharging process. The former is caused by lattice expansion/contraction due to ion insertion,[12] while the latter results from Zn stripping/plating. In particular, ~1.7 μm mAh^{-1} will be produced in Zn anode theoretically, which could reach ~5 μm mAh^{-1} in practice because of the loose deposition morphology.[3c, 13] The combined effects of the above actions can deform hydrogel electrolytes by over 50%, especially at high cycling capacity, and the deformation percentage will be aggravated in thinner hydrogel electrolytes that are necessitated in commercial cells. This poses a significant challenge to compressive ability and anti-fatigue properties for long-term cycling.

PAM-based hydrogel electrolytes have been widely explored due to their high elasticity, which could be further boosted through the incorporation of a second polymer phase, such as CMC,[14] carboxymethyl chitosan[15] and [2-(methacryloyloxy) ethyl]dimethyl-(3-sulfopropyl) (SBMA).[16] In particular, the carboxymethyl chitosan incorporation has enabled the excellent low-temperature performance.[15] The resulting dual-network hydrogel exhibits more tensile elongation than pure PAM hydrogel. Nevertheless, the performances of Zn-ion cells using hydrogel electrolytes are still unsatisfactory at high current rates and long-term cycles (**Table S1**). The underlying reasons may reside in the poor mechanical stability under compression and the failure of hydrogel during cyclic loading, both of which lack an in-depth study for correlating them with hydrogel integrity and cell stability. Therefore, we systematically explore the anti-fatigue feature of PAM-based hydrogel electrolytes under repeated compression and the corresponding Zn deposition behavior by tuning the salt and the crosslinking of the

copolymer. Delightedly, a $Zn(ClO_4)_2$-PAM-chitosan electrolyte (C-PAMCS) has been developed, endowing Zn anode with an unprecedented cyclic lifespan of over 1500 h under a high current rate and capacity of 10 mA cm^{-2}/10 mAh cm^{-2}. In addition, such an electrolyte is well compatible with wearable technologies, as demonstrated by the all-flexible batteries with excellent deformability. We reveal that the anti-fatigue property is crucial to achieving high-capacity Zn metal anodes, thus adding another dimension to hydrogel electrolyte design.

2. Results and Discussions

2.1. Mechanical property of hydrogel electrolyte

The one-pot preparation process of C-PAMCS is schematically illustrated in **Figure 1c**. Specifically, a homogeneous precursor solution containing acrylamide (AM) monomer, chitosan chains (CS), Zn^{2+} source, ammonium persulfate (APS) initiator, and N, N'-methylenebisacrylamide (MBA) crosslinker was poured into the mold and thermally polymerized at 60 ℃ for 2 hours. Note that during the preparation process, the 2 M $Zn(ClO_4)_2$ salt was directly added to the precursor solution before crosslinking rather than using the conventional soaking method. The reason is that the residual active water molecules on the surface of the soaked hydrogel will trigger dendrite formation and parasitic reactions at the interface.[17] In addition, different from the conventional soaking method, the water content of hydrogel electrolytes synthesized by our method is controlled at ~50% for each patch of electrolytes (**Figure S2a-b**), which endows the hydrogel with better mechanical properties (**Figure S2c-d)**. For comparison, the pure PAM hydrogel without the addition of CS is also prepared with the same strategy (denoted as C-PAM). The digital images in **Figure 1d** demonstrate the C-PAMCS formation from liquid precursor to transparent film. The optical image of the hydrogel surface (**Figure S3a)**, and cross-sectional/top-view SEM of freeze-dried hydrogel **(Figure 3, Figure S3b)** show that the C-PAMCS network exhibits a continuous three-dimensional architecture and interconnected homogeneous pore structures, facilitating water

confinement and Zn^{2+} ion transport. Compared to the C-PAM network with a much loose pore structure (**Figure S4**), such a dual network is also expected to deliver improved mechanical properties. The chemical composition and bonding information of hydrogel matrices are examined by Fourier transform infrared spectroscopy (FT-IR) (**Figure 1f**). C-PAM and C-PAMCS networks exhibit similar FT-IR patterns with various peak intensities assigned to the stretching vibration of the functional groups and the further hydrolysis of amide groups.[18] The C-PAM network exhibits peaks at 3340 cm^{-1} and 3194 cm^{-1} for the stretching vibrations of N-H, 1655 cm^{-1} for C=O stretching, 1605 cm^{-1} for N-H deformation, and 1099 cm^{-1} for $-NH_2$ in-plane rocking vibrations. As for the C-PAMCS network, the adsorption peaks for N-H stretching and $-NH_2$ in-plane rocking vibrations shift to 3320 cm^{-1} and 1118 cm^{-1}, respectively, attributed to the formation of intermolecular hydrogen bonds between PAM chains and CS chains.[19]

Subsequently, the mechanical properties of hydrogel electrolytes are evaluated. After the addition of CS chains, the tensile strength of the C-PAMCS reaches 50 kPa with an enhanced failure strain of 1200%, over twice that for C-PAM with a relatively low tensile strength of 19 kPa (**Figure 2a**). Such a high ductility is sufficient to avoid premature failure of flexible devices caused by inevitable deformations in daily activities. Turning to the compression test, as shown in **Figure 2b-c**, the compressive stress of C-PAM decreases sharply at about 90% strain, possibly due to localized structural damage. In contrast, C-PAMCS exhibits a much higher rigidity because of the increased crosslinking of the polymer chains. Smooth stress-strain curves and pronounced hysteresis loops for compressive strains up to 90% are observed, indicating energy dissipation by the viscoelastic hydrogel.

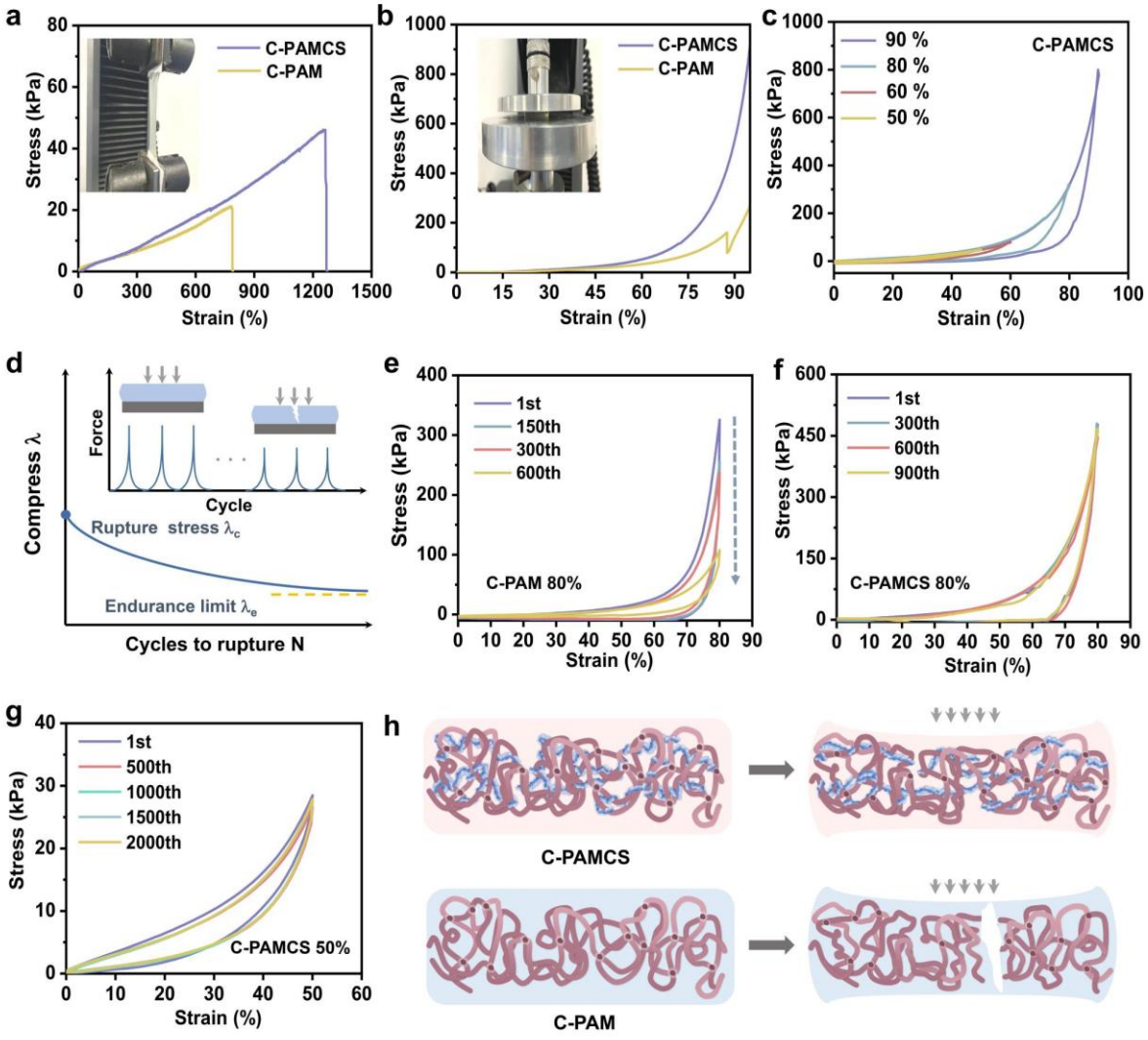

Figure 2. Mechanical tests of hydrogel electrolytes. (a) Tensile and (b) compressive stress-strain curves of C-PAM and C-PAMCS; (c) Compressive stress-strain curves of C-PAMCS under various strains; (d) Cyclically load a sample without an initial cut to the amplitude of compress, λ, and record the number of cycles to rupture, N; Stress-strain curves of successive compression cycles under 80 % strain for (e) C-PAM and (f) C-PAMCS; (g) Stress-strain curves of successive compression cycles under 50 % strain for C-PAMCS; (h) Illustration of the network structures of the C-PAM and C-PAMCS before and after compressing to fracture.

Since Zn plating/stripping poses repeated stresses to the hydrogel electrolyte, a sound anti-fatigue property is critical for long-term cycling. The principle for the fatigue test is shown in **Figure 2d**. The sample without cracks is cyclically compressed to a given stress amplitude λ,

and the number of cycles N for failure is recorded.[20] Specifically, below the rupture stress amplitude λ_c, the damage of the hydrogel aggravates with the increase of stress amplitude, reflected by the decreases of cycling numbers N. λ_e is the endurance limit, below which the material is able to withstand countless cycles of fatigue without failure. In fact, only a few papers have thus far appeared in the literature on compressive fatigue of hydrogels.[21] Under continuous loading-unloading compressive cycles, **Figure S5a** and **Figure 2e** show that C-PAM experiences an almost linearly declining force-cycle relationship over the whole testing, in agreement with the crack formation at an early stage (inset of **Figure S5a**). In the following cycles, the continuously decreased stress is induced by the propagation and/or multiplication of cracks, leading to the failure of the hydrogel within merely 600 cycles. By contrast, C-PAMCS presents a clear division at around 900 cycles between the almost plateau and the linearly declining force-cycle curves (**Figure S5b and Figure 2f**). There is an absence of any obvious crack until 900 cycles, after which the cracks propagate/multiply with continuous cycles. Encouragingly, at a mild strain of 50%, a 2000-loop test can still be realized without any damage to C-PAMCS (**Figure S6** and **Figure 2g**).

The potential mechanism for the distinct responses of the two different hydrogels to compressive fatigue loading is demonstrated in **Figure 2h**. The single-network C-PAM lacks a toughening mechanism to dissipate mechanical energy so that the compressive load will immediately cause damage until the cracks trigger a failure only after several hundred cycles. However, the mechanical stress is effectively dissipated in the as-prepared C-PAMCS. By sliding the physical entanglement points along the chains or deforming the network conformation, the CS chains effectively absorb the energy arising from the compressive stress to prevent the crack from growing to a macroscopic level.[22]

2.2. Zn plating/stripping behavior

In addition to mechanical properties, dendrite suppression and parasitic reaction inhibition capability of the hydrogel electrolyte are also crucial for vigorous and stable Zn anodes. The kinetics and corrosion-resistance features of the C-PAMCS are first disclosed by electrochemical measurements. As illustrated in **Figure 3a**, 2M $Zn(ClO_4)_2$ aqueous electrolyte (AE) exhibits an ionic conductivity of 31.6 mS cm^{-1},[23] slightly decreasing to 23.1 mS cm^{-1} and 22.6 mS cm^{-1} for C-PAM and C-PAMCS, respectively. It shows that polymerization has a mild impact on ionic conductivity. The electrochemical windows of various electrolytes are evaluated in **Figure 3b-c**. Compared to AE, the hydrogen evolution reactions (HER) and oxygen evolution reactions (OER) of C-PAM and C-PAMCS are all retarded, suggesting the improved corrosion-resistance ability.[24] This is also confirmed by the X-ray diffusion (XRD) results. After 10 cycles, the byproduct peak at 11.8°, attributed to $Zn_4ClO_4(OH)_7 \cdot nH_2O$ (PDF#41-0715), is examined on the XRD pattern of Zn anode with AE.[4b] In comparison, the Zn anodes with C-PAM and C-PAMCS exhibit anti-corrosion capability, evidenced by the negligible byproducts detected (**Figure 3d**).

Turning to the deposition behavior, the Zn^{2+} diffusion can be reflected in d*I* (current)-d*t* (time) curves, which are recorded under an overpotential of -200 mV (**Figure 3e**). As for symmetric cells with AE, the continuously changed d*I*/d*t* beyond 300 s signifies a random diffusion, resulting in frantic dendrite growth. On the contrary, the constant value of dI/dt close to zero suggests a steady diffusion for both C-PAM and C-PAMCS.[25] Such uniform diffusion of Zn^{2+} can be schematically explained by diffusion pathways of Zn^{2+} ions in **Figure 3f**. For instance, C-PAMCS network possesses a strong interaction of polar Zn and higher binding energy with Zn atom than the Zn surface.[10] The interaction between C-PAMCS and Zn^{2+} is further explored by density functional theory (DFT) calculation. As displayed in **Figure S7**, the average binding energy of Zn^{2+} with acyl group and hydroxyl group (-1.57 eV) is larger than that with H_2O (-1.07 eV) and Zn surface (-0.70 eV). It indicates that Zn^{2+} tends to be captured

by polymer, which helps uniform Zn^{2+} transport from the electrolyte to the anode surface. Benefiting from above merits, the Zn^{2+} transference number in C-PAM and C-PAMCS are enhanced to 0.63 and 0.69 compared to 0.44 for aqueous electrolytes (**Figure S8**).

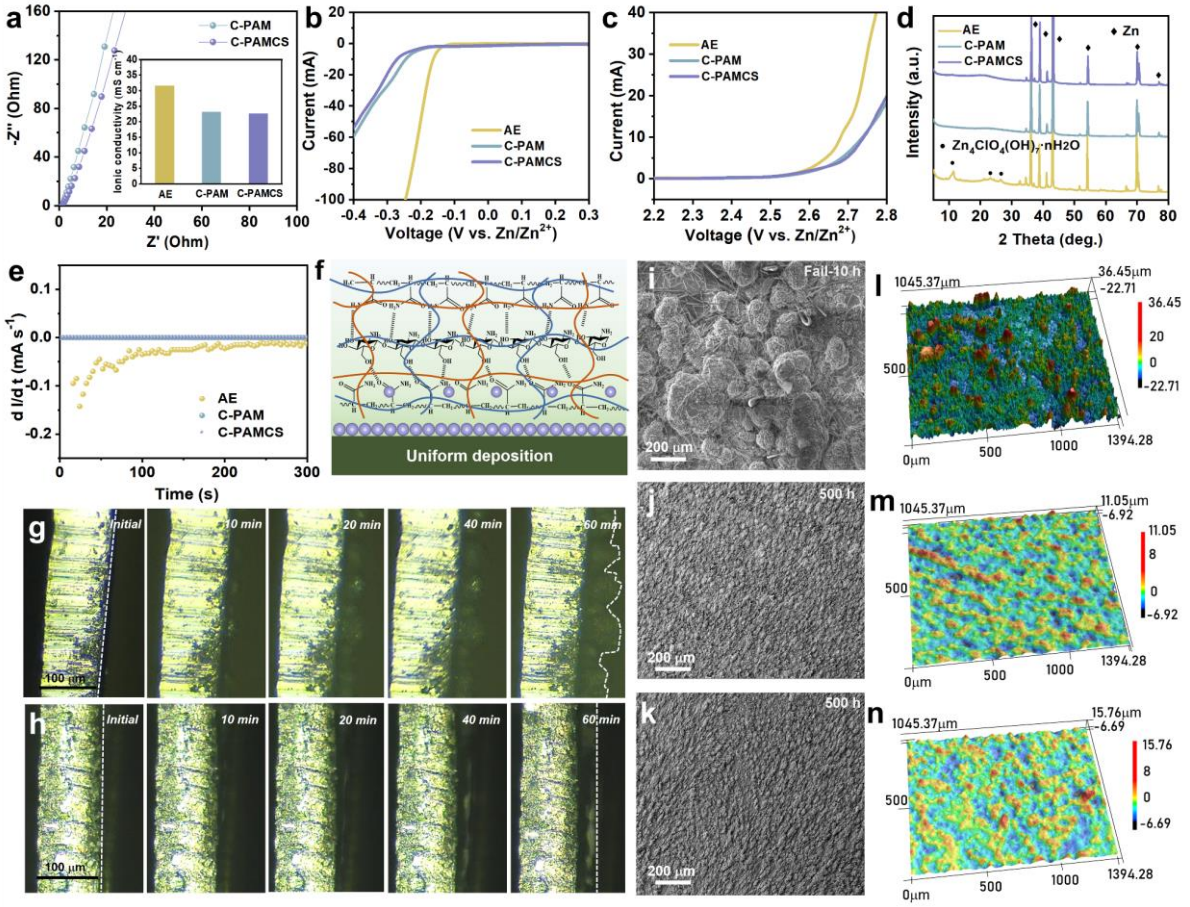

Figure 3. Corrosion and deposition behavior. (a) Electrochemical impedance spectroscopy (EIS), (b) HER and (c) OER curves of various electrolytes; (d) XRD pattern of Zn anodes with various electrolytes after cycling; (e) d*I*/d*t* curves for symmetric cell with various anodes under a constant voltage of -200 mV; (f) Schematic illustration of Zn^{2+} deposition mechanism in C-PAMCS; In situ optical microscopy images of Zn plating in (g) AE and (h) C-PAMCS; SEM images of Zn anode after cycling with (i) AE, (j) C-PAM and (k) C-PAMCS; and corresponding CLMS images in (l) AE, (m) C-PAM and (n) C-PAMCS.

The distinct diffusion behaviors would greatly impact the Zn deposition morphology, which is examined in Zn//Zn symmetric cells with various electrolytes. Firstly, in-situ optical

microscopy was employed to track the deposition of Zn under a current density of 10 mA cm^{-2}. As shown in **Figure 3g-h**, both Zn foils in the aqueous electrolyte and C-PAMCS display a smooth surface at the beginning of the Zn plating. In the aqueous electrolyte, small and loose Zn particles could be observed on the Zn surface after 10 min electrodeposition, then gradually evolving into a thick and uneven convex dendrite layer after 60 min. In contrast, Zn foil with C-PAMCS electrolyte exhibits a stable surface morphology throughout the entire plating process. No signs of dendrites or pulverization are detected, illustrating that the designed hydrogel electrolyte facilitates uniform Zn deposition. Then, SEM images of Zn surface in a wide field of view after cycling are collected to ensure the authentic surface features. Specifically, short circuit occurs for the cell with AE only after 10 h, resulting from the randomly distributed bulges observed on the surface of Zn anode (**Figure 3i**). By contrast, with C-PAM and C-PAMCS, it is encouraging to find that the Zn foil surface forms uniform morphology even after 500 h without dendrite growth (**Figure 3j-k**). Confocal laser microscopy (CLMS) images were collected to demonstrate the 3D topography of Zn anode. With AE, apparent dents and humps can be observed on the Zn anode surface with the maximum height difference of more than 60 μm (**Figure 3l**). On the contrary, a much smaller surface height fluctuation (≈20 μm) of cycled Zn in C-PAM and C-PAMCS implies that the hydrogel effectively induces flat deposition after the long-term operation of 500 h (**Figure 3m-n**).

2.3. Stability of Zn metal anode

The above analysis shows that the incorporation of CS into PAM maintains the advantage of hydrogel in guiding the uniform Zn deposition while boosting the mechanical stability upon cyclic loading. We then explore the effect on the long-term electrochemical stability in symmetric Zn//Zn cells. As expected, both C-PAM and C-PAMCS highly improve the cyclic life of Zn anode compared to AE because of the uniform Zn deposition. The cell with AE suffers a sudden short circuit at 70 h when cycling at a current density of 5 mA cm^{-2} and capacity of 5

mAh cm^{-2}, much inferior to ~2100 h for C-PAM, which could be further improved to ~2700 h for C-PAMCS (**Figure 4a**). The benefits of C-PAMCS are more clearly exemplified by the performance under 10 mA cm^{-2}/10 mAh cm^{-2}, delivering a stable cycling of more than 1500 h, twice that of the cell with C-PAM (**Figure 4b**). The reason lies in the increased stress under a high cycling capacity. About 5 μm of Zn thickness increase will be induced for 1 mAh Zn deposition, making the maximum elastic compression strain and the anti-fatigue property of great importance to the cell stability, the reason why C-PAMCS delivers much better performance than C-PAM.

Remarkably, the cell with C-PAMCS delivers a lifespan of 700 h at a challenging capacity of 30 mAh cm^{-2} (**Figure 4c**). In comparison, the C-PAM-based cell fails within 360 h, again confirming the vital role of mechanical stability under high-capacity cycling. Such an outstanding performance at high rates and cyclic capacity is hardly achieved in the hydrogel electrolyte prepared by the conventional soaking method (**Figure S9**). The accumulative capacity (ACC.) of symmetrical Zn cells with C-PAMCS can reach 15000 mAh cm^{-2} at 10 mA cm^{-2} (**Figure 4d** and **Table S1**), which surpasses most Zn anodes based on hydrogel electrolytes employing polymer matrices including carboxymethyl chitosan and PAM (CSAM-C),[15] 3-((2-(methacryloyloxy)ethyl)dimethylammonio) propane-1-sulfonate and PAM (ADC-GEL),[26] PAM-poly (ethylene glycol) diacrylate-CMC (PMC),[14] poly 2-acrylamido-2-methyl-1-propane sulfonate zinc (PAMSZN),[27] cellulose nanofibril (MorpgGE),[28] poly(3-(1-vinyl-3-imidazolio) propanesulfonate) and bacterial cellulose (PZIB),[29] PAM-dimethylsulfoxide (PDZ-H),[8] ionic liquid-PAM (IL-PAM),[30] tannic acid modified SA (TA-SA),[6] agarose-PAM-CMC (SHE),[31] gelatine-alginate (GAME),[32] and PVA-CMC.[33]

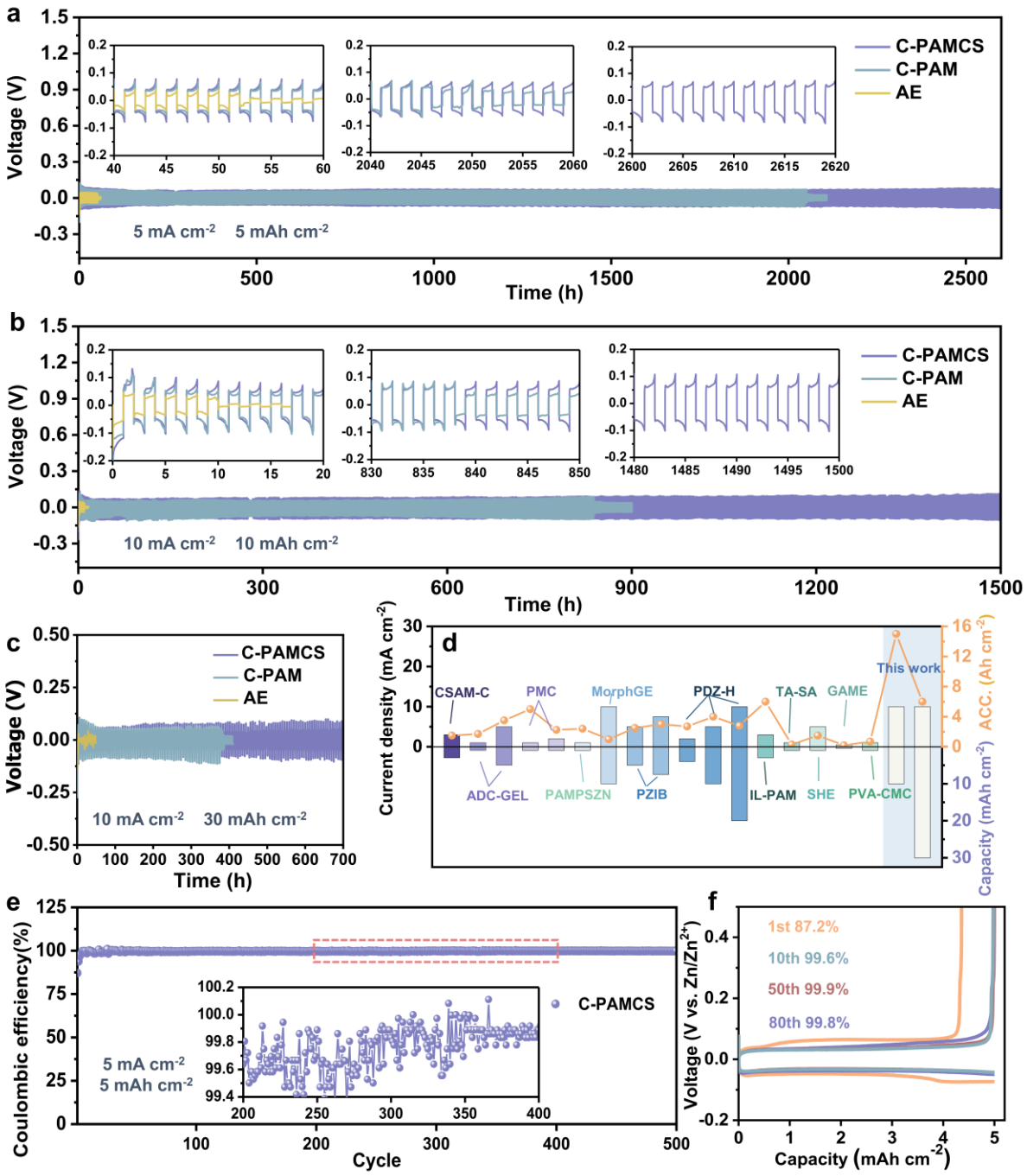

Figure 4. Cyclic performance and reversibility of Zn anode. Voltage profiles of the symmetric cell at (a) 5 mA cm^{-2}/5 mAh cm^{-2}, (b) 10 mA cm^{-2}/10 mAh cm^{-2}, and (c) 10 mA cm^{-2}/30 mAh cm^{-2}; (d) Performance comparison of C-PAMCS and other reported hydrogel in terms of current densities, specific capacities, and accumulative capacities; (e) Coulombic efficiency of Zn//Cu cell with C-PAMCS at 5 mA cm^{-2} and (f) corresponding voltage profiles.

The reversibility of Zn plating/stripping behavior is further investigated by the coulombic efficiency (CE) test under Zn//Cu asymmetric cells. Encouragingly, after a short active process, the cell with C-PAMCS displays an impressive average CE of over 99.8% for 500 cycles with extraordinarily steady plating/stripping voltage profiles (**Figure 4e-f**). The high CE can still be maintained at a high value of 99.6-99.9% at 2 mA cm^{-2}/2 mAh cm^{-2} and 10 mA cm^{-2}/10 mAh cm^{-2}, outperforming most of the reported hydrogel electrolytes (**Figure S10** and **Table S1**). Thanks to the impressive reversibility, the cells could also run at a large depth of discharge (DOD) to improve the Zn utilization (**Figure S11**). In detail, a Zn//Cu cell was assembled employing C-PAMCS with 10 mAh of Zn first deposited on the Cu side. The cell sustains over 400 h under 6 mA cm^{-2}/6 mAh cm^{-2} (60% DOD).

2.4. The rationale for hydrogel electrolyte design

Having confirmed the exceptional performance of C-PAMCS, we then explore the underlying principle for the rational design of hydrogel electrolyte. The above analysis assures that the damage to hydrogel electrolytes is one of the essential factors affecting the properties of the Zn anode. The load cycle curve (**Figure S3**) indicates that the fracture mechanism of as-prepared hydrogel electrolyte follows the double linear damage rule (DLDR) theory, which is developed from the Miner's rule (**Figure S12**).[34] Briefly, fatigue damage is divided into two stages. That is, in the crack formation stage,

$$\sum n_i/(a_i N_i) = 1 \quad (1)$$

in the crack propagation stage,

$$\sum m_i/[(1-a_i)N_i] = 1 \quad (2)$$

where *n* and *m* are the number of cycles in the fatigue crack formation and propagation stages, respectively; *a* is the proportion of the crack formation stage in the total number of cycles. Given the crack forms almost immediately after the fatigue loading (**Figure 2e** and **Figure S3a**), it is assumed that the damage accumulation for C-PAM is dominated by the crack propagation stage. This means that both *n* and *a* are close to zero and only Equation (2) applies

in analogy to the original Miner's rule. The incorporation of CS brings about two phases of damage accumulation through both crack formation and propagation stages. Therefore, both the *n* and *m* values significantly increase for delaying the crack formation and impeding the crack propagation while *a* becomes a finite value between zero and unity, according to the DLDR theory (**Figure S12**). As the cracks in hydrogel electrolyte may induce micro-short-circuit of the battery, it is envisaged that the unique capability of C-PAMCS to mitigate fatigue damage would be more advantageous.

We then explore the strategy to delay the crack formation, which is the key to extending the hydrogel and cell life under repeated deformation. Firstly, along with the polymer matrix, salt is a crucial factor that should be considered in the design of hydrogel electrolytes. In this regard, another two popular salts, $ZnSO_4$ and $Zn(CF_3SO_3)_2$, are adopted to prepare the PAMCS-based hydrogel electrolytes, which are denoted as S-PAMCS and O-PAMCS, respectively. Although these two salts do not alter the Zn deposition morphology (**Figure S13**), they exhibit much inferior anti-fatigue property. As demonstrated in **Figure S14,** both S-PAMCS and O-PAMCS sustain less than 400 compression cycles at a maximum of 80% strain, compared to ~900 cycles for C-PAMCS. This is because the chaotropic anions ClO_4^- can dissociate the hydrogen bond, improving the mechanical flexibility of the hydrogel to prevent crack formation.[35] Apart from the improved mechanical stability, the $Zn(ClO_4)_2$ offers other merits in ionic conductivity and low-temperature performance (detailed in **Figure S15-16**). The above results emphasize the salt effect, in addition to the copolymer matrix, on the anti-fatigue properties.

Apart from CS, other second polymer phases like polyvinyl alcohol (PVA) and gelatin (GE) are also expected to deliver an analogous effect benefiting from the effective energy dissipation. Therefore, based on $Zn(ClO_4)_2$, we prepare the polyacrylamide-polyvinyl alcohol (C-PAMPVA), and polyacrylamide-gelatin (C-PAMGE) hydrogel electrolytes following the same procedure and investigate their mechanical properties and the resulting Zn metal anode

performance. Indeed, incorporating a second polymer phase could greatly enhance the bond connections, leading to a dense network similar to C-PAMCS (**Figure S17**). Consequently, the C-PAMPVA and C-PAMGE exhibit a much longer compression cycle than C-PAM under 80% maximum strain (**Figure S18**). Nevertheless, the cells based on C-PAMPVA and C-PAMGE show a poor cyclic life of no more than 200 h when cycling at 5 mA cm^{-2}/5 mAh cm^{-2} and 10 mA cm^{-2}/10 mAh cm^{-2} (**Figure S19**). We speculate that such a significant difference is due to the rough deposition morphology of Zn metal under the two hydrogel electrolytes (**Figure S20**). Zn metal has a high modulus of ~108 GPa,[36] much larger than that of PAM-based hydrogel. The sharp Zn edges induced by the non-uniform growth in C-PAMPVA and C-PAMGE may easily penetrate the hydrogel and promote the crack formation, leading to their quick failure.

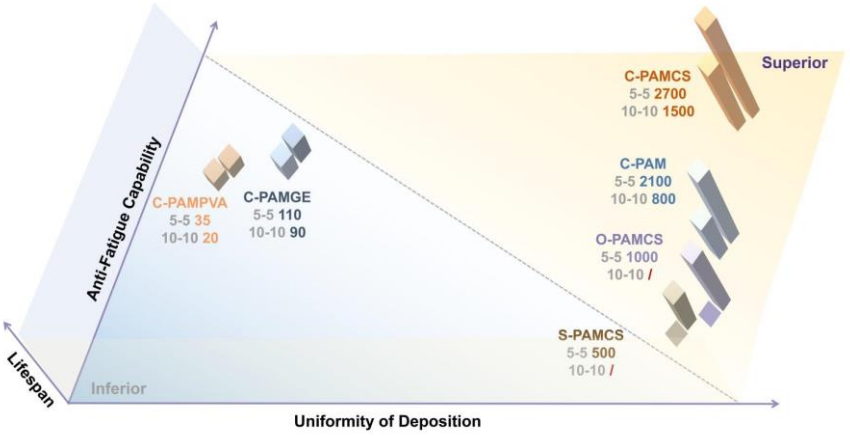

Figure 5. Illustration of the correlation between the performance and deposition uniformity and anti-fatigue capability (i. e. "5-5 2700" means symmetric cells can be operated for 2700 h under 5 mA cm^{-2}/5 mAh cm^{-2}).

We illustrate the two critical parameters, i.e., deposition morphology and mechanical stability, in achieving long-lifespan and high-capacity Zn metal anode (**Figure 5**). In general, the dual-network hydrogel could greatly improve the anti-fatigue property by dissipating the energy during cyclic loading. Nevertheless, such an enhancement must be retained on the premise of ensuring uniform deposition. Unlike traditional hydrogel, a salt has to be incorporated for application in the battery, which may deteriorate the mechanical stability.

Fortunately, some chaotropic anions, like ClO_4^-, assist in disrupting the hydrogen bond to benefit the stability under repeated deformation. Based on these principles, the C-PAMCS is optimal owing to the uniform Zn deposition and enhanced anti-fatigue property at large strain.

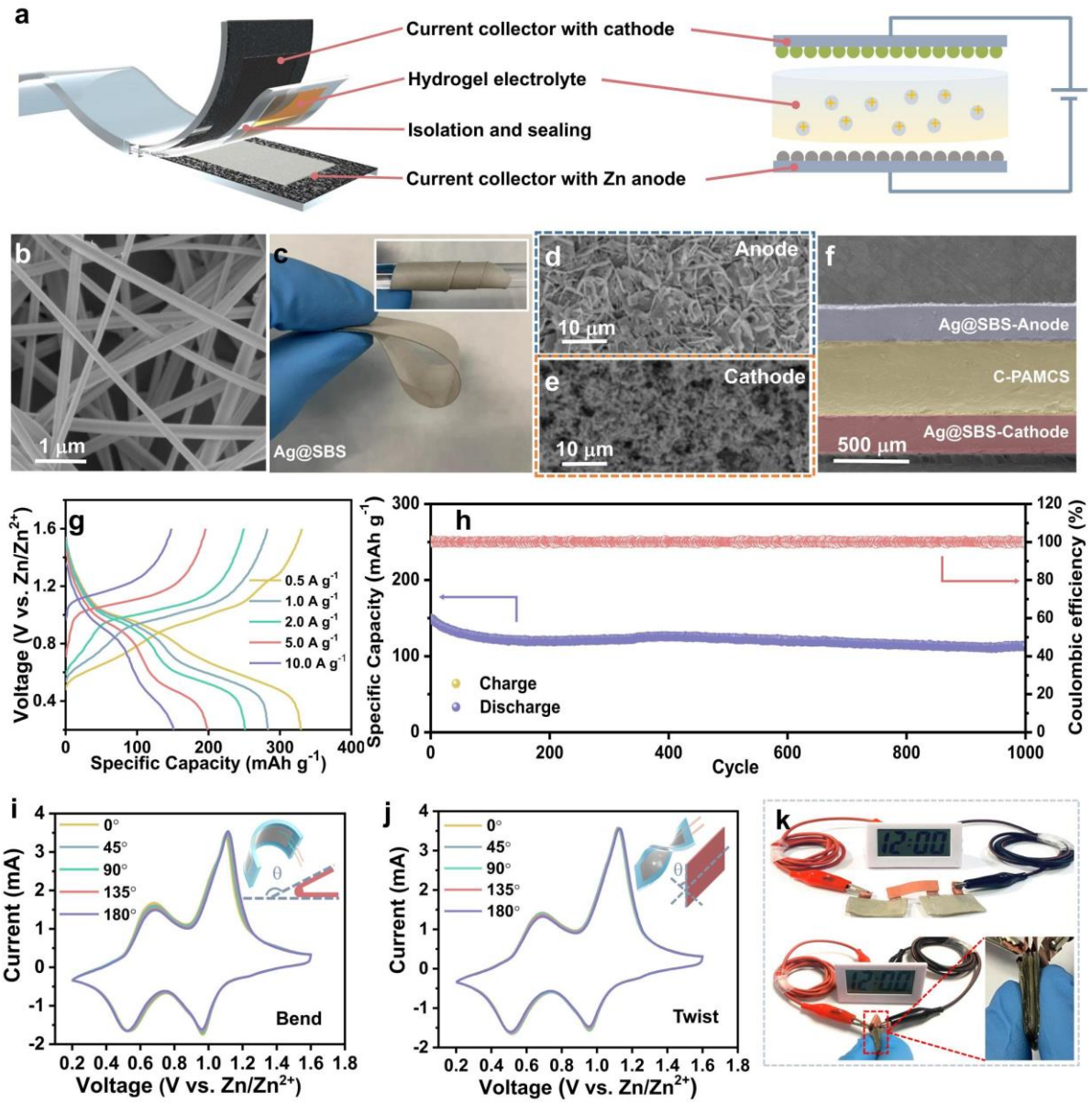

Figure 6. Assembly and performance of the all-flexible cell. (a) The structure of the proposed cell; (b) SEM of synthesized AgNWs; (c) Digital images of Ag@SBS current collector; SEM of (d) Zn anode and (e) $Cu_xV_2O_5{\cdot}nH_2O$ cathode; (f) Cross-sectional SEM image of flexible cell; (g) Voltage profiles under various current rates; (h) Cyclic performance at 10 A g^{-1}; CV curves under (i) bending and (j) twisting status at various angles; (k) Photographs of electronic watch powered by two-in-series cells.

2.5. All-flexible batteries

Encouraged by the great mechanical stability of C-PAMCS, we further examine its performance in all-flexible Zn ion batteries to explore the practical application in growing smart and wearable electronics. The structure of the proposed all-flexible battery is schematically depicted in **Figure 6a**. The styrene-butadiene-styrene block polymer (SBS) is selected as the matrix of the current collector owing to its high flexibility, chemical stability, and biocompatibility.[37] The electron transfer paths are constructed by integrating Ag nanowires (AgNWs) with a diameter of 20 nm and length of 5 μm (**Figure 6b**). The detailed fabrication procedure is illustrated in **Figure S21a**. Firstly, AgNWs are dispersed uniformly and coated on a glass mold. The SBS solution is then coated over the AgNWs network and dried to obtain a freestanding film (Ag@SBS), where the AgNWs are distributed evenly on the smooth SBS surface with a thickness of 5 μm (**Figure S21b-d**, and **Figure 6c**).

Afterward, the Zn anode is prepared through electrodeposition of Zn nanosheets on the Ag@SBS with a mass loading of 2-3 mg cm^{-2} (**Figure 6d**). Turning to the cathode, the V_2O_5 microsphere co-inserted by the Cu^{2+} and H_2O molecules (denoted as $Cu_xV_2O_5{\cdot}nH_2O$) is prepared by the conventional hydrothermal method,[38] which is cast on the Ag@SBS (**Figure 6e**). The resulting cathode and anode are uniform and flexible with low resistances of 21 Ohm cm^{-1} and 1.5 Ohm cm^{-1}, respectively (**Figure S22**). Finally, the Zn anode, C-PAMCS, and cathode are assembled layer by layer with intact contact, as shown in cross-sectional images (**Figure 6f**). Note that a relatively thick hydrogel electrolyte is adopted because of the processability in the homemade device. After being sealed by SBS film, the flexible cell is obtained for the electrochemical tests. The rate performance of the flexible cell operated at current densities from 0.5 to 10 A g^{-1} is presented in **Figure 6g**. The stable capacities of 330, 283, 250, 195, and 147 mAh g^{-1} are obtained at current densities of 0.5, 1.0, 2.0, 5.0, and 10.0 A g^{-1}, respectively. The capacities of the device return to the nearly initial value after the current

reduces to 0.5 A g^{-1}, indicating its excellent electrochemical reversibility (**Figure S23**). Even under a high current density of 10 A g^{-1}, the device can be operated for 1000 cycles, maintaining a decent retention rate of 76.8% and nearly 100% CE (**Figure 6h**). The hydrogel electrolyte does not sacrifice the rate capability and cycling stability compared to the aqueous electrolyte (**Figure S24**). The designed hydrogel electrolyte also benefits stability at a small current density by partly inhibiting the cathode dissolution and suppressing the electrolyte decomposition (**Figure S25**).

Impressively, the device maintains a capacity of over 100 mAh g^{-1} when a limit Zn source is preset at a negative-to-positive (N:P) electrode capacity ratio of 2:1 (**Figure S26**). The cyclic voltammetry (CV) curves at different bending and twisting angles are illustrated in **Figure 6i-j**. The two pairs of cathodic/anodic peaks associated with the Zn^{2+} insertion/extraction behavior are almost overlapped at different deformation states. The shape-preserved CV curves suggest the negligible performance decay under various bending angles from 0° to 180°, demonstrating its mechanical flexibility and reliability.[39] The flexibility of full cells under repeated bending and twisting cycles is evaluated in **Figure S27**. The cells show similar capacity retention as those cycling in normal conditions. As a proof-of-concept demonstration, two cells are connected in series, which deliver an average voltage of over 1.5 V (**Figure S28**). **Figure 6k** displays photographs of an electronic watch powered by two-in-series devices, showing promising potential for flexible energy storage systems.

3. Conclusion

Through systematic studies of Zn anodes employing various hydrogel electrolytes, we have shown that the anti-fatigue property plays a vital role in guaranteeing the stability and integrity of hydrogel. Both the salt and polymer matrix significantly affect the mechanical stability of hydrogel under cyclic compression. Among all the synthesized electrolytes, the engineered C-PAMCS stands out to be an ideal choice for high-energy Zn anodes. Thanks to the chaotropic

salt and dual-network copolymer, the C-PAMCS shows improved anti-fatigue properties without sacrificing the Zn deposition homogeneity. As a result, the symmetric Zn//Zn cell employing C-PAMCS delivers unprecedented cyclic life at a large capacity, i.e., more than 2700 h and 1500 h at 5 mA cm^{-2}/5 mAh cm^{-2} and 10 mA cm^{-2}/10 mAh cm^{-2}, respectively. In addition, a high average coulombic efficiency of 99.8% is obtained, evidencing the excellent Zn deposition/stripping reversibility and the capability of suppressing parasite reactions. The potential of such an anti-fatigue hydrogel electrolyte is demonstrated in an all-flexible Zn-ion battery enabled by Ag@SBS current collectors. The battery exhibits remarkable flexibility and stability that would be attractive for powering wearable electronics.

Supporting Information

Supporting Information is available from the Wiley Online Library or from the author.

Acknowledgements

This work was supported by the General Research Fund (GRF) scheme of the Hong Kong Research Grants Council (Project No. 15307221) and the Hong Kong Polytechnic University (CDBJ & ZE2F).

Received: ((will be filled in by the editorial staff))

Revised: ((will be filled in by the editorial staff))

Published online: ((will be filled in by the editorial staff))

References

[1] a)K. K. Fu, J. Cheng, T. Li, L. Hu, *ACS Energy Lett.* **2016**, 1, 1065; b)Y. Jia, Q. Jiang, H. Sun, P. Liu, D. Hu, Y. Pei, W. Liu, X. Crispin, S. Fabiano, Y. Ma, Y. Cao, *Adv. Mater.* **2021**, 33, e2102990; c)X. Chi, M. Li, J. Di, P. Bai, L. Song, X. Wang, F. Li, S. Liang, J. Xu, J. Yu, *Nature* **2021**, 592, 551; d)X. Xiao, X. Xiao, Y. Zhou, X. Zhao, G. Chen, Z. Liu, Z. Wang, C. Lu, M. Hu, A. Nashalian, S. Shen, K. Xie, W. Yang, Y.Gong, W. Ding, P. Servati, C. Han, S. X. Dou, W. Li, J. Chen, *Sci. Adv.* **2021**, 7, eabl3742.

[2] a)J. M. Tarascon, M. Armand, *Nature* **2001**, 414, 359; b)J. Kim, I. Jeerapan, J. R. Sempionatto, A. Barfidokht, R. K. Mishra, A. S. Campbell, L. J. Hubble, J. Wang, *Acc. Chem. Res.* **2018**, 51, 2820.

[3] a)X. Gao, H. Zhang, X. Liu, X. Lu, *Carbon Energy* **2020**, 2, 387; b)H. Li, C. Han, Y. Huang, Y. Huang, M. Zhu, Z. Pei, Q. Xue, Z. Wang, Z. Liu, Z. Tang, Y. Wang, F. Kang, B. Li, C. Zhi, *Energy Environ. Sci.* **2018**, 11, 941; c)Q. Liu, Y. Wang, X. Hong, R. Zhou, Z. Hou, B. Zhang, *Adv. Energy Mater.* **2022**, 12; d)Z. Hou, Y. Gao, H. Tan, B. Zhang, *Nat. Commun.* **2021**, 12, 3083.

[4] a)J. Shin, J. Lee, Y. Park, J. W. Choi, *Chem. Sci.* **2020**, 11, 2028-2044; b)V. Verma, S. Kumar, W. Manalastas, M. Srinivasan, *ACS Energy Lett.* **2021**, 6, 1773; c)A. Chen, C. Zhao, J. Gao, Z. Guo, X. Lu, J. Zhang, Z. Liu, M. Wang, N. Liu, L. Fan, Y. Zhang, N. Zhang, *Energy Environ. Sci.* **2022**, DOI: 10.1039/d2ee02931f.

[5] a)K. Zhao, G. Fan, J. Liu, F. Liu, J. Li, X. Zhou, Y. Ni, M. Yu, Y. M. Zhang, H. Su, Q. Liu, F. Cheng, *J. Am. Chem. Soc.* **2022**, 144, 11129; b)C. Li, A. Shyamsunder, A. G. Hoane, D. M. Long, C. Y. Kwok, P. G. Kotula, K. R. Zavadil, A. A. Gewirth, L. F. Nazar, *Joule* **2022**, 6, 1103; c)S. Guo, L. Qin, T. Zhang, M. Zhou, J. Zhou, G. Fang, S. Liang, *Energy Storage Mater.* **2021**, 34, 545.

[6] B. Zhang, L. Qin, Y. Fang, Y. Chai, X. Xie, B. Lu, S. Liang, J. Zhou, *Sci. Bull.* **2022**, 67, 955.

[7] Y. Zhang, Y. Chen, X. Li, M. Alfred, D. Li, F. Huang, Q. Wei, *J. Power Sources* **2021**, 482, 228963.

[8] H. Lu, J. Hu, L. Wang, J. Li, X. Ma, Z. Zhu, H. Li, Y. Zhao, Y. Li, J. Zhao, B. Xu, *Adv. Funct. Mater.* **2022**, 32, 2112540.

[9] J. Shin, J. Lee, Y. Kim, Y. Park, M. Kim, J. W. Choi, *Adv. Energy Mater.* **2021**, 11, 2100676.

[10] Q. Zhang, J. Luan, L. Fu, S. Wu, Y. Tang, X. Ji, H. Wang, *Angew. Chem. Int. Ed.* **2019**, 58, 15841.

[11] S. Wen, C. Luo, Q. Wang, Z. Wei, Y. Zeng, Y. Jiang, G. Zhang, H. Xu, J. Wang, C. Wang, J. Chang, Y. Deng, *Energy Storage Mater.* **2022**, 47, 453.

[12] a)Y. Liu, Z. Dai, W. Zhang, Y. Jiang, J. Peng, D. Wu, B. Chen, W. Wei, X. Chen, Z. Liu, Z. Wang, F. Han, D. Ding, L. Wang, L. Li, Y. Yang, Y. Huang, *ACS Nano* **2021**, 15, 9065; b)J. C. Stallard, L. Wheatcroft, S. G. Booth, R. Boston, S. A. Corr, M. F. L. De Volder, B. J. Inkson, N. A. Fleck, *Joule* **2022**, 6, 984.

[13] L. Yuan, J. Hao, C.-C. Kao, C. Wu, H.-K. Liu, S.-X. Dou, S.-Z. Qiao, *Energy Environ. Sci.* **2021**, 14, 5669.

[14] P. Lin, J. Cong, J. Li, M. Zhang, P. Lai, J. Zeng, Y. Yang, J. Zhao, *Energy Storage Mater.* **2022**, 49, 172.

[15] S. Huang, L. Hou, T. Li, Y. Jiao, P. Wu, *Adv. Mater.* **2022**, 34, 2110140.

[16] W. Zhang, F. Guo, H. Mi, Z. S. Wu, C. Ji, C. Yang, J. Qiu, *Adv. Energy Mater.* **2022**, 12, 2202219.

[17] Y. Qin, H. Li, C. Han, F. Mo, X. Wang, *Adv. Mater.* **2022**, 34, 2207118.

[18] Q. Liu, C. Xia, C. He, W. Guo, Z. P. Wu, Z. Li, Q. Zhao, B. Y. Xia, *Angew. Chem. Int. Ed.* **2022**, 61, e202210567.

[19] a)W. Kong, C. Wang, C. Jia, Y. Kuang, G. Pastel, C. Chen, G. Chen, S. He, H. Huang, J. Zhang, S. Wang, L. Hu, *Adv. Mater.* **2018**, 30, e1801934; b)X. Liang, B. Qu, J. Li, H. Xiao, B. He, L. Qian, *React. Funct. Polymers* **2015**, 86, 1.

[20] R. Bai, J. Yang, Z. Suo, Eur. *J. Mech. A Solids* 2019, 73, 337.

[21] a)A. Joshi, G. Fussell, J. Thomas, A. Hsuan, A. Lowman, A. Karduna, E. Vresilovic, M. Marcolongo, *Biomater.* **2006**, 27, 176; b)L. Xu, C. Wang, Y. Cui, A. Li, Y. Qiao, D. Qiu, *Sci. Adv.* 5, eaau3442; c) Q. Li, L. Wang, Q. Liu, W. Hong and C. Yang, *Front. Robotic AI* **2021**, 8, 666334.

[22] J. P. Gong, Y. Katsuyama, T. Kurokawa, Y. Osada, *Adv. Mater.* **2003**, 15, 1155.

[23] R. Rajabi, S. Sun, A. Billings, V. F. Mattick, J. Khan, and K. Huang, J. Electrochem. Soc. 2022, 169, 110536

[24] Y. Sui, X. Ji, *Chem. Rev.* **2021**, 121, 6654.

[25] Z. Zhao, J. Zhao, Z. Hu, J. Li, J. Li, Y. Zhang, C. Wang, G. Cui, *Energy Environ. Sci.* **2019**, 12, 1938.

[26] Q. He, G. Fang, Z. Chang, Y. Zhang, S. Zhou, M. Zhou, S. Chai, Y. Zhong, G. Cao, S. Liang, A. Pan, *Nano-micro Lett.* **2022**, 14, 93.

[27] J. Cong, X. Shen, Z. Wen, X. Wang, L. Peng, J. Zeng, J. Zhao, *Energy Storage Mater.* **2021**, 35, 586.

[28] F. Cao, B. Wu, T. Li, S. Sun, Y. Jiao, P. Wu, *Nano Research* **2021**, 15, 2030.

[29] Y. Hao, D. Feng, L. Hou, T. Li, Y. Jiao, P. Wu, *Adv. Sci.* **2022**, 9, e2104832.

[30] J. Huang, X. Chi, Y. Du, Q. Qiu, Y. Liu, *ACS Appl. Mater. Interfaces* **2021**, 13, 4008.

[31] W. Ling, F. Mo, J. Wang, Q. Liu, Y. Liu, Q. Yang, Y. Qiu, Y. Huang, *Mater. Today Phy.* **2021**, 20, 100458.

[32] Y. Lu, T. Zhu, N. Xu, K. Huang, *ACS Appl. Energy Mater.* **2019**, 2, 6904.

[33] X. Zhu, C. Ji, Q. Meng, H. Mi, Q. Yang, Z. Li, N. Yang, J. Qiu, *Small* **2022**, 18, e2200055.

[34] a)S. S. Manson, G. R. Halford, *Int. J. Fracture*, **1981**, 17, 169; b)K. Hectors, W. De Waele, *Metals* **2021**, 11, 204.

[35] Y. Shang, C. Wu, C. Hang, H. Lu, Q. Wang, *Adv. Mater.* **2020**, 32, e2000189.

[36] J. Zheng, Q. Zhao, T. Tang, J. Yin, C. D. Quilty, G. D. Renderos, X. Liu, Y. Deng, L. Wang, D. C. Bock, C. Jaye, D. Zhang, E. S. Takeuchi, K. J. Takeuchi, A. C. Marschilok, L. A. Archer, *Science* **2019**, 366, 645.

[37] a)L. Tang, J. Shang, X. Jiang, *Sci. Adv.* **2021**, 7, eabe3778; b)Z. Ma, Q. Huang, Q. Xu, Q. Zhuang, X. Zhao, Y. Yang, H. Qiu, Z. Yang, C. Wang, Y. Chai, Z. Zheng, *Nat. Mater.* **2021**, 20, 859.

[38] Q. Liu, Z. Yu, R. Zhou, B. Zhang, *Adv. Funct. Mater.* **2023**, 33, 2210290,

[39] L. E. Blanc, D. Kundu, L. F. Nazar, *Joule* **2020**, 4, 771.